npj | flexible electronics

Article

Published in partnership with Nanjing Tech University

https://doi.org/10.1038/s41528-025-00518-0

Conformal, ultrathin crystalline-silicon-based Hall sensor arrays with deep learning models for early-stage monitoring of three-dimensional tumor tissues

Junhan Liu[1,2,3,14], Zhongyuan Wu[1,2,3,14], Lianjie Zhou[1,2,3,14] ✉, Yanran Shen[4], Xiaojun Wu[1,2,3], Junling Liang[5], Yuting Shao[6], Pengchuan Liu[1,3], Zhongzheng Li[1,3], Bofan Hu[1,3], Ming Wang[2], Zengfeng Di[7], Tianjun Cai[1,3], Fan Xu[8], Su Jiang[9,10], Mengdi Han[11], Ling Tao[4] ✉, Yongfeng Mei[1,3,12] & Enming Song[1,2,3,9,13] ✉

Dynamic dimension assessments of tumor tissues have broad relevance in clinical diagnosis and the treatment of patients. Current technologies for such a purpose include quasi-static measurements that lack microscale resolution and sensing sites, with limited capabilities for time-dependent, three-dimensional profiling of tumors, particularly at the early growth stage. Here, we report the conformal Hall-sensor-based systems for continuous monitoring of tumor morphological features such as growth rates and volumes. Such platforms incorporate ultrathin crystalline-silicon nanomembranes (200 nm thick) as a basis for displacement sensing via magnetic flux detection, in an array design that yields spatiotemporal information of tumor geometries at high sensitivity. Evaluation involves real-time measurements on a living mouse model with tumor tissues at various pathological conditions, where the integration with deep learning algorithms can further enable the system for large-scale tumor profile reconstruction across tissue surfaces. These microsystems provide the potential for monitoring of tumor progression and treatment guidance in patients.

Technologies capable of establishing in vivo dimension assessment of tumor tissues represent a grand scientific challenge, with paramount significance in biomedical research as well as clinical practice in human healthcare[1,2]. An important focus is to dynamically capture tumor geometric features, especially volume and growth rate, that can provide essential information particularly at early stage[3–5]. Specifically, subtle increases in tumor volume are an early biomarker of malignancy, as they precede detectable metabolic or genomic changes and signal the onset of angiogenesis, providing a critical window for early diagnosis. The rate of this volumetric growth directly indicates tumor aggressiveness and prognosis, allowing for non-invasive risk stratification between benign and malignant lesions[6–9]. Conventional means in this context include quasi-static measurements of displacements under invasive forces such as applied indentation, suction, torsion or compression[10–12]. Non-invasive methods include advanced imaging techniques (e.g., computed tomography and magnetic resonance imaging) that yield quantitative spatial-temporal information of tumor morphology[13–16]. Although promising, these approaches typically involve large associated equipment within hospital settings, thus precluding their use as patients' wearables for continuous, precise monitoring of targeted tumor tissues and for at-home diagnostics under dynamic conditions[17]. For such purposes, critical challenges still remain in the development of miniaturized, lightweight electronic systems, in wearable/implantable formats, that enable in vivo morphological characterization during tumor growth with time-dependent measurements of tumor geometric features.

Recent reports have described the developments of state-of-the-art electronic platforms for capturing micro-deformation of the tumor surface during early-stage progression of the malignant cancerous tissues, across measurement scales of millimeter levels[18–22]. Examples range from a metal-film strain gauge for evaluation of tumor size under therapy, to HfO_2-nanoparticle-based wearable sensor for monitoring tumor volumes within weeks, and to needle-shaped optoelectronics for calibrating tumor diameters during different growth stages[23–25]. These and other systems utilize

A full list of affiliations appears at the end of the paper. ✉e-mail: ljzhou@fudan.edu.cn; ling_tao@fudan.edu.cn; sem@fudan.edu.cn

thin, flexible device architectures that intimately interface with deformable tissue surfaces, at various scales that range from the cellular level to macroscopic coverages in a minimally invasive manner[26]. In many cases, however, these bioelectronic platforms only provide measurement capabilities with insufficient sensing sites and displacement resolution of tumor dimensions, thereby limiting their applications for dynamically mapping complex topography across cancerous tissues at early pathological stages.

The novelty of Hall sensors can offer functional integration possibilities in this context, with powerful measurement capabilities of micro-displacement and orientation, at a wide range of measurement scales[27–30]. Nevertheless, these technologies typically involve the rigid, planar modules that inevitably introduce significant uncertainties when operating on curved surfaces, not amenable to wearable designs with mechanical compliance[31,32]. A key consideration is to establish the engineered design capable of bending, stretching, and twisting during contact with soft, time-dependent biological tissues, thereby reducing mechanical mismatch at the biotic/abiotic interface while maintaining operational stability. Recent studies reported flexible, thin-film Hall sensors for characterization of tiny distance changes and angular variations under magnetic fields[33–37]. Constituent materials usually include bismuth (Bi), gallium arsenide (GaAs), and indium antimonide (InSb) to other two-dimensional materials such as graphene[38–44]. As a comparison, the well-established semiconductor Hall sensor, such as silicon, can provide superior system functionalities, with stable performance, high levels of biocompatibility and low device-to-device variability[27,45,46].

Here, we report the development and applicability of the flexible, wearable Hall sensor for monitoring tumor growth dynamics via recording weak magnetic flux variations, in an array design that is capable of high-precision mapping geometrical parameters (e.g., height, volume, morphology). The device integrates the ultrathin, transferred silicon nanomembranes (Si-NMs, 200 nm thick) serving as the functional elements that can enable intimate contact on targeted tumor surfaces, capturing the magnetic signals related to dimension information during tumor growth. Experimental and simulation studies establish the optimized device design of the Hall sensors with the measurement sensitivity as 4.41 V/A T and the minimum detection limit as low as 1 μT, and evaluate their performance across representative wearable applications and dynamic conditions. As an example, the device can mount on the tumor surface of a living mouse under gradient magnetic fields, yielding continuous monitoring of tumor height variation at micro-scale at the early stage of tumor growth. Integration of array designs and deep learning architectures with convolutional neural network enables large-area mapping over tissue surfaces to quantify tumor volumes, with enhanced measurement capability using a residual neural network for three-dimensional profiling. These results create future opportunities for clinic use with continuous monitoring of tumor progression and the capability of early-stage pathological diagnosis and in-time treatments.

Results

Materials, designs, and operation principles of the flexible Si-based Hall sensor

Figure 1a presents the schematic illustration and operation principle of the device, which we refer to as the flexible Si-based Hall (FSH) sensor, serving as a skin-mounted wearable platform for physiological magnetic signal monitoring, capable of being seamlessly interfaced with dynamic biological tissues. The stack structure appears in Fig. 1a(i). Here, the ultra-thin monocrystal silicon nanomembrane (Si-NM, 200 nm thick) forms the Hall element, connected by four metal electrodes (Cr/Au, 10 nm/100 nm thick). The fabrication begins with the transfer printing of Si nanomembrane (Fig. S1) from boron-doped (~10^{20} atoms/cm^3) p-type Silicon-on-insulator (SOI, SOITEC) wafer onto the pre-cured polyimide (PI) film (5 μm thick) on a temporary glass substrate, followed with sequences of lithographic patterning, etching, and integration with metal wire connection, and then encapsulated by another PI film layer (5 μm thick). The following release of the sensor from the temporary glass substrate and printing onto a polydimethylsiloxane (PDMS) substrate (30 μm thick, elastic modulus of 750 kPa) using water-soluble tape to establish the wearable platform for biomagnetic sensing. More information about the fabrication process details can be found in "Methods" section and Fig. S2. Figure 1a(ii) shows the operation principle of the FSH sensor based on the Hall effect. Specifically, the constant voltage or current is biased on one couple of electrodes (source electrodes) to generate moving charge carriers, which accumulate in one side of Si-NM under the Lorentz force in the magnetic field, thus generating Hall voltage collected by another couple of electrodes (Hall electrodes).

Notably, the specific geometrical shuttle shape of the Si-NM is the optimized result of finite element analysis (FEA) simulations and validated by experimental results in Fig. 1b, c. Among the three shapes of cross, rectangle and shuttle that have been widely reported[36,47–49], the experimental result reveals that the shuttle shape is able to generate the strongest Hall voltage signal in the constant magnetic field compared to the other two (Fig. S3), consistent with the relevant works reported before[49,50]. According to the principles of electrostatic charge distribution, charge density tends to accumulate more highly at sharp geometric features in semiconductors. In a shuttle-shaped structure, this effect causes charge carriers to concentrate at the tapered ends of the Hall electrodes, thereby generating an enhanced Hall voltage due to the geometric focusing of electric fields[50]. The FEA results on the comprehensive investigation about the geometric dimensions (i.e., cross ratio, aspect ratio, taper angle, and electrode length) define the optimized structures of each of the three shapes (Figs. S4–S7). The optimal geometrical design of the shuttle shape maintains the necessary contact length along the long edge while gradually tapering the width towards the short edge in a triangular form, as shown in optical images of Fig. 1d. The overall aspect ratio (L/W) of the shuttle shape retains 3:1 (300 μm length, 100 μm width) to reach the maximum geometrical factor for better sensitivity[49], while the Hall electrodes contact the sharp corner ($\tan\theta/2 = 5/8$) to enhance the Hall voltage[50]. Furthermore, the same batch of FSH sensors exhibits highly consistent response to magnetic field (Fig. S8), with negligible performance degradation after transferring to flexible substrates (Fig. S9), demonstrating the potential of the fabrication process to scale up to wafer dimensions. The epidermal FSH sensor shown in Fig. 1e exhibits seamless dermal conformability with preserved interface stability on the fingertip. The results of repeated attachment/detachment tests are summarized in Fig. S10. For the peel strength measurement (90° peel angle) between FSH sensors and human skin (Fig. S10a), the adherence force as a function of displacement is shown in Fig. S10b. The average adherence force to the surface decreases from an initial value of 0.07 N to 0.04 N after 20 attachment/detachment cycles, but is restored after gentle cleaning with ethanol and deionized water. The calculated adhesion energy values in the three states are 2.38 J/m^2, 1.37 J/m^2, and 2.30 J/m^2 (Fig. S10c), comparable to those of PDMS-based wearable electronics measured in related literature[51], which also means the repeatedly used FSH sensor can maintain the original adhesion energy as the pristine condition after cleaning. Furthermore, the Hall voltage response exhibits minor variation under a constant magnetic field (80 mT) throughout the repeated attachment tests (Fig. S10d), confirming that mechanical reattachment has a negligible impact on the electrical interface. For the long-term drift test with biofluid exposure, the devices ($N = 3$) are attached on fresh and damp pork skin sprayed by artificial sweat (Fig. S11a), in conditions of constant temperature (37 °C) and high humidity (85%). Figure S11b shows the Hall voltage recorded under a constant magnetic field (80 mT). The devices still work, though the normalized signal exhibiting a total drift of 15% over 15 days. This can be compensated for by a calibration procedure prior to testing.

For the mechanical performance of FSH sensors, Fig. 1f displays the optical images of the sensor on an artificial skin substrate (PDMS, 0.5 mm thick) at various mechanical deformation states and corresponding theoretical simulation, which include bending (with a bending radius of 10 mm), twisting (with a twisting angle of 90°), and stretching (Fig. S12, with an elongation of 10%). The internal strain distributions of the FSH sensor are analyzed by finite element analysis (FEA) simulation (Table S1). In both conditions of bending and twisting, the simulated results show that the maximum strain in the Si-NM and metal wires is less than 2%, well below

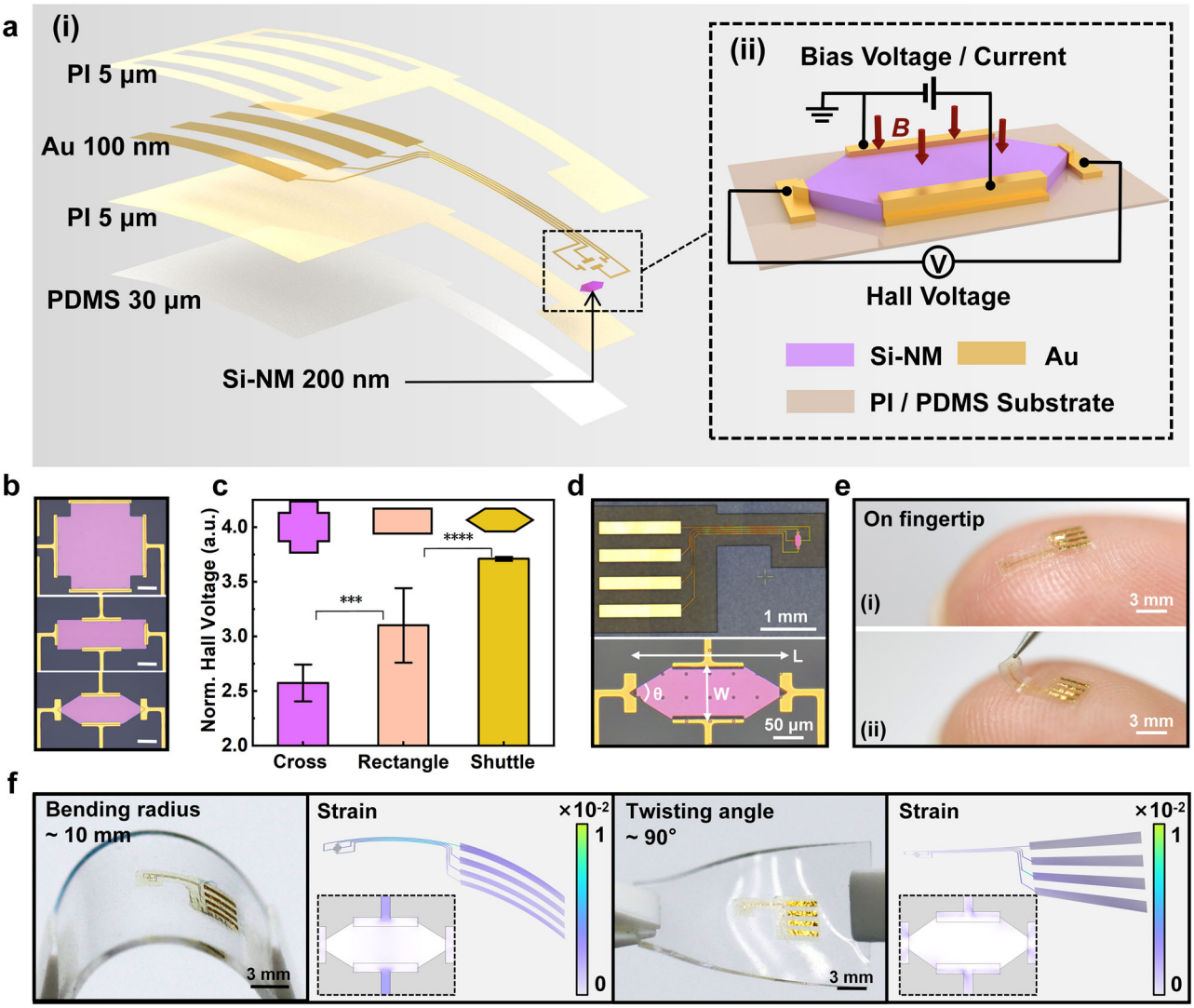

Fig. 1 | Materials, designs, and operation principles of the flexible Si-based Hall (FSH) sensor. a (i) Exploded layered structure diagram of the FSH sensor and (ii) Enlarged view of the device area with operational schematic. **b** Photographs of the various Si-NM shape. Top: Cross. Middle: Rectangle. Bottom: Shuttle. Scale bar: 50 μm. **c** Comparison of the Hall voltage signal amplitude with the Si-NM shape of the cross, rectangle and shuttle. Error bars represent SD ($n = 10$). **d** Optical images of the over view (top) and the geometrical details (bottom) of the FSH sensor. **e** Photographs of a transferred FSH sensor (i) seamlessly laminated on the fingertip and (ii) nondestructive detachment from the fingertip. **f** Optical images of the FSH sensor under different modes of mechanical deformation, including bending at the radius of 10 mm and twisting at the angle of 90°, as well as the corresponding FEA results of strain distribution across the Si-NM (the inset) and metal wires. The ns (no significance) $p > 0.05$, $^{*}p < 0.05$, $^{**}p < 0.01$, $^{***}p < 0.001$, $^{****}p < 0.0001$.

the critical fracture strain of Si (5%) and gold film (7%)[52,53], suggesting the excellent flexibility and mechanical robustness. Further analysis (Fig. S13) reveals that the strain is constrained within PDMS substrate due to the mechanical property mismatch (i.e., Young's modulus) between Si-NM (170 GPa), gold (70 GPa), PI (3.1 GPa) and PDMS (750 kPa), thereby effectively eliminating the strain within the FSH sensor[54]. More details and results of the FEA simulation can be found in "Methods" section. These results of excellent mechanical stability are essential to ensure the functional integrity and operational effectiveness of the FSH sensor in dynamic environment of Internet of Things (IoT) and diverse biomedical scenes.

Device characteristics of FSH sensor for in vitro magnetic field monitoring

Application-oriented magnetic fields include both fixed unidirectional magnetic field and dynamically induced electromagnetic field with various frequency, which places higher demands on the performance of the FSH sensor. Figure 2a illustrates the response of the FSH sensor to alternating magnetic fields (20–200 μT, 50 Hz–100 kHz) generated via a Helmholtz coil, with field parameters precisely controlled by a signal generator (Fig. S14). More experimental details can be found in "Methods". Quantitative analysis reveals a distinct linear proportionality ($R^2 > 0.99$) between signal amplitude and magnetic field at constant frequencies. This linear relationship allows that the signal can be feasibly calibrated, and thus enabling effective detection of unknown environmental magnetic fields in real-world sensing applications. Concurrently, frequency-modulated enhancement of voltage output is observed under fixed field intensities (Fig. S15). This frequency-dependent behavior aligns with Faraday's electromagnetic induction principles, where the induced electromotive force scales linearly with oscillation frequency[55]. Figures 2b and S16 display the time-resolved detection of weak magnetic fields (50–200 μT) with amplitude modulation. Here, 0.1 Hz square wave signal drives the alternating magnetic field with a 10-s period, with the field strength controlled by the signal amplitude, which can be clearly distinguished by the Hall voltage variation of FSH sensors. Under our detection condition, the sensor exhibits rapid state transitions (response/recover time <2 s) to guarantee the real-time monitoring requirements for transient magnetic phenomena

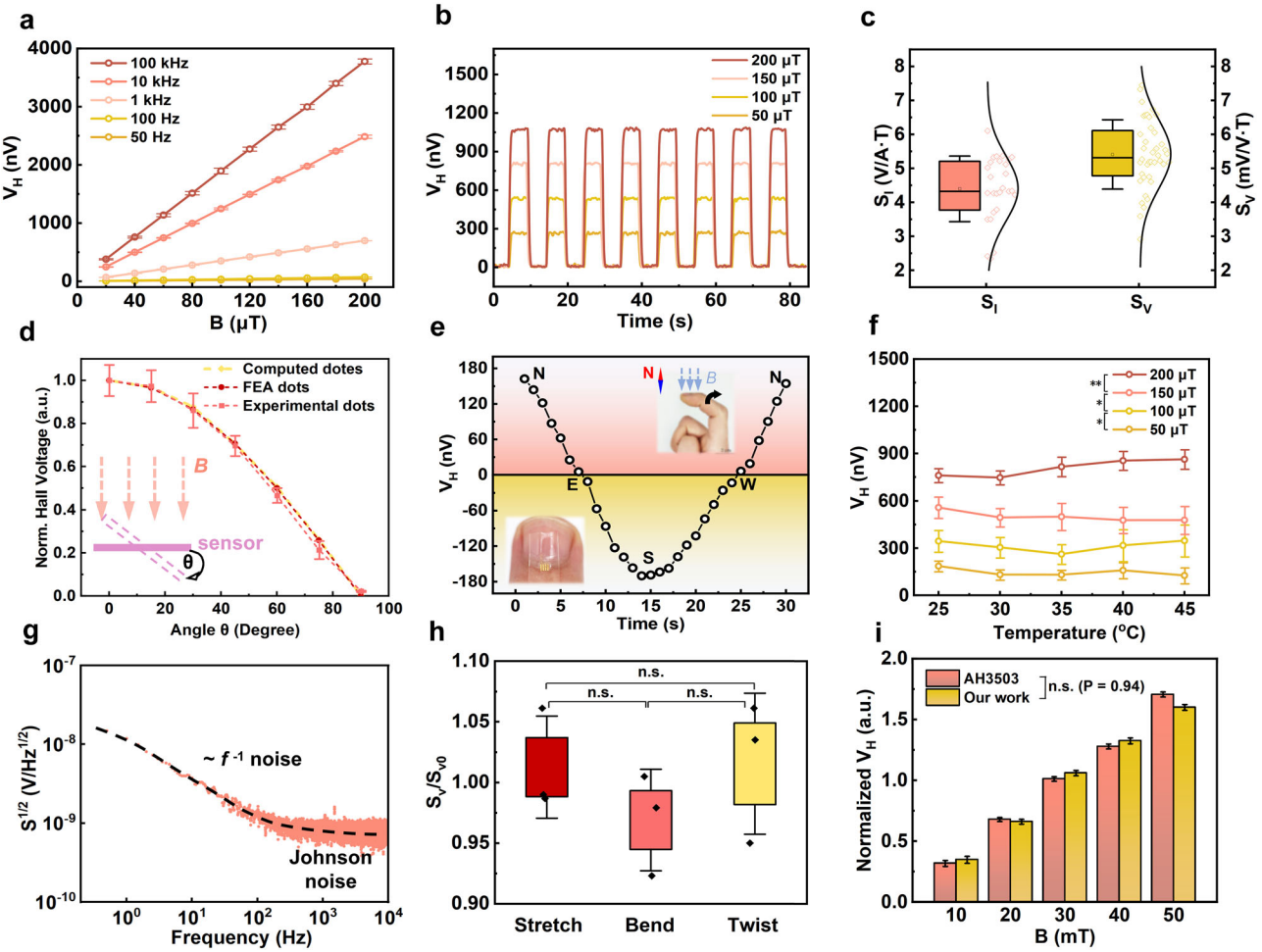

Fig. 2 | Device characteristics of the FSH sensor and its monitoring of magnetic fields and direction. a Line graph of Hall voltage variation with weak magnetic field at different frequencies. **b** The sensor response in time scale under weak magnetic fields of 50–200 μT. **c** The current sensitivity (S_I) and voltage sensitivity (S_V) of the same batch of the sensors. Curve: Normal Distribution. **d** Comparison between the theoretical calculated values (yellow line), FEA values (red line), and the experimental values (pink line) for the FSH sensor subjected to constant magnetic fields at variable directions. **e** The FSH sensor attached to the fingernail serves as the direction detector for the geomagnetic field. **f** The performance stability of the FSH sensors against fluctuating environmental temperature. **g** Noise spectra of the FSH sensors obtained through FFT, with a bias current of 1 mA. **h** Hall sensitivity variation after 1000 cycles deformation tests. **i** Comparison of the Hall voltage signals of the FSH sensor and commercial Hall elements (AH3503) under mT-level magnetic fields. Error bars represent SD ($n \geq 3$). The ns (no significance) $p > 0.05$, $^{*}p < 0.05$, $^{**}p < 0.01$, $^{***}p < 0.001$, $^{****}p < 0.0001$.

while maintaining amplitude discrimination fidelity across the operational range (Fig. S17). The current sensitivity (S_I, defined as Hall voltage output per unit magnetic field and bias current) and voltage sensitivity (S_V, defined as Hall voltage output per unit magnetic field and bias voltage) of the same sensor batch adhere to the Gaussian distribution with a mean value of 4.41 V/A T and 5.42 mV/V T respectively (Fig. 2c), both of which are comparative to those of the industrialized silicon-based Hall sensors reported before[45]. Table S2 presents a performance comparison of the Si-NM-based Hall sensor with other Hall sensors reported before. Compared to flexible but low-sensitivity Bi-film sensors and high-sensitivity yet rigid/toxic GaAs/InSb-based sensors, Si-NM-based Hall elements achieve a superior balance between performance and biocompatibility[36,44,56].

Alternatively, the Hall voltage not only depends on the magnetic field strength but also on the angle between the magnetic flux density vector and the sensor plane. The angle dependence reveals in the following Formula 1 describing the balance between Lorentz force and the electric field force:

$$q \cdot \frac{V_H}{d} = qv_0B_z = qv_0B \cdot \cos\theta \quad (1)$$

where q is the quantity of electric charge, V_H is the Hall voltage, d is the distance between the Hall electrodes, v_0 is the charge transport velocity, B_z is the vertical component of the magnetic field strength, B is the total magnetic field strength, and θ is the angle between the magnetic vector and the normal vector of sensor plane. Accordingly, V_H is proportional to $\cos\theta$, thus enabling direction detection under nearly constant external magnetic field. The sketch in Fig. 2d shows that the sensor rotates in a constant field with rotation angle θ. The Hall voltage captured by the sensor during rotation (pink line) closely aligns with the theoretical calculation result of Formula 1 (yellow line) and the FEA results (red line), with the Pearson's correlation coefficient (r) of 0.99812 and 0.99818, demonstrating the reliability of the experimental results. In addition, the FSH sensor demonstrates wearable magnetometric functionality through biomechanically integrated compass operation on the fingertip (Fig. 2e). The calibration process is to identify the geomagnetic north alignment, corresponding to the direction of maximum signal amplitude of the FSH sensor. The direction detection starts with the geomagnetic field entering the sensor plane vertically (north), followed by the finger attached with the sensor rotating 360° within 30 s. The Hall voltage reveals strict angular dependency, peaking at geomagnetic north alignment before decreasing to the null point at east orientation. Subsequent

rotation induces polarity inversion, achieving negative saturation at south alignment, following a cosinusoidal angular dependence as the Hall effect theory and Formula 1. Those results illustrate the capability of FSH sensors for autonomous geomagnetic vector mapping.

To illustrate the stable device performance, the FSH sensor remains a stable signal output under various temperatures ranging from 25 °C to 45 °C (Fig. 2f), with a negligible thermal-resistivity effect that excludes the influence induced by the fluctuating environmental temperature. Figure 2g examines the electrical noise within the sensors under measurements, where the voltage noise power spectrum with a bias current of 1 mA exhibits the noise behavior in broad frequency bands (10^{-1} Hz–10^{4} Hz). The result indicates that in low-frequency range, the noise has a nearly liner decrease, showing the apparent feature of 1/*f* noise that commonly dominates in this frequency band[57,58]. As the frequency increases to higher than 10^{2} Hz, the noise spectrum flattens out, indicating the transition from 1/*f* noise to Johnson noise. In this instance, the minimum detection limit of Hall sensors can be defined as the noise equivalent magnetic field (NEMF) as the following Formula 2[59]:

$$NEMF\,(f) = \frac{\sqrt{S_f}}{S_I \cdot I} \tag{2}$$

where f is the frequency, S_f is the noise power spectral density, I is the current, and S_I is the current sensitivity of the Hall sensor. According to Formula 2, at the frequency of higher than 10^{2} Hz, the minimum detection limit of the FSH sensor is below 1 μT with the bias current of 1 mA, which is much lower than the average geomagnetic field (~40 μT), thus revealing the potential of geomagnetic field detection. To validate the performance stability during deformations, systematic electromechanical tests covering stretching, bending, and twisting modes, each repeated across three independent devices ($N = 3$) are conducted. The real-time resistance of the FSH sensor is recorded while applying controlled deformation of bending (radius of 10 mm), twisting (90°), and uniaxial stretching (20%). Taking advantage of the intrinsic piezoresistive behavior of monocrystalline Si-NMs[60,61], the resistance change directly reflects the mechanical strain experienced by the Si-NM[62]. As shown in Fig. S18a–c, the normalized resistance traces remain within ±0.5% variation under all deformation conditions during 1000 deformation cycles, indicating that the operational strain range remains well below the fracture limit and that no permanent damage occurs. To directly link mechanical deformation to sensing performance, the Hall sensitivity is further quantified before and after repeated mechanical cycling. As summarized in Fig. 2h, the average voltage sensitivity (S_V) remains above 95% of the initial value (S_{V0}) for all three deformation modes, with variation within 10% across multiple devices. These results indicate the stable robustness of the FSH sensor under different mechanical conditions, thereby satisfying the demands for magnetic field detection on curved surfaces without notable performance degradation. Figure 2i shows the signal of the FSH sensor in response to mT-level magnetic fields generating by a permanent magnet, exhibiting similar variation trends by comparison with commercial Hall elements (AH3503). With the capability of integrated directional/field dual-mode sensing and mechanical flexibility, the FSH sensor effectively enables as a transformative platform for bio-magnetic interaction studies and conformal wearable magneto electronics.

Principle and operation of FSH sensors for tumor growth monitoring in animal models

Pathological changes, especially for tumor growth, can lead to variation of tumor volume in vivo, triggering tiny deformation and displacement of tissue surfaces[8]. The FSH sensors can characterize the physiological information of tumors via monitoring of those tiny but critical geometrical parameter changes (e.g., tumor height) associated with the initial progression of tumors, thus achieving necessary early warning and postoperative monitoring. Figure 3a shows the FSH sensor attached to the tumor on the left side of the mouse, while the inset provides a magnified view to demonstrate the seamless and conformal device attachment. The tumor is induced by the SK-N-BE(2) cell line (Fig. S19), which is injected on the left side of the mouse in advance, with the FSH sensor mounting on the injection region. Measurements of the FSH sensor follow with placing the magnet 20 mm precisely above the injected site to generate a constant magnetic field. Detailed experimental processes can be found in the "Methods" section. Figure 3b shows the cross-section illustration of the micro-displacement caused by early stage of tumor growth. As the tumor develops, the tumor-related tissue surface deforms and raises the sensor at the top of tumor closer to the magnet, thereby resulting in the increasing signals recorded by the FSH sensor, which can allow for continuous monitoring of the tumor height during growth.

The calibration process of tumor height measuring is conducted by collecting Hall voltage signal at a function of various distances between the sensor and magnet, with the experimental setup illustrated in the inset of Fig. 3c and the fitting standard curve in Fig. S20. The initial distance between the sensor and magnet is 20 mm and gradually decreases to 10 mm due to the upward displacement of the sensor. The Hall voltage signal increases as the sensor approaches the magnet by orders of magnitudes (from 0.9 μV to 139 μV), where larger displacement can lead to the stronger signal, as expected. This can be explained by the expression for the axial magnetic field distribution of the permanent magnet used in our experiment, according to the current model in magnetostatic analysis[63–65]:

$$B(z) = \frac{\mu_0 \mu_r M_0}{2}\left[\frac{z+t}{\sqrt{R^2+(z+t)^2}} - \frac{z}{\sqrt{R^2+z^2}}\right] \tag{3}$$

where μ_0 is the magnetic permeability of the vacuum, μ_r is the relative magnetic permeability of the medium, M_0 is the magnetization, z is the distance to the magnet, t is the magnet thickness, and R is the magnet radius. The Hall voltage can be expressed as:

$$V_H = v_0 d \cos\theta \cdot \frac{\mu_0 \mu_r M_0}{2}\left[\frac{z+t}{\sqrt{R^2+(z+t)^2}} - \frac{z}{\sqrt{R^2+z^2}}\right] \tag{4}$$

where v_0 is the charge transport velocity, d is the distance between two Hall electrodes, and θ is the angle between the magnetic vector and the normal vector of sensor plane. Here, the normalized V_H of Formula 4 (the red line) shares the consistent variation trend with experimental V_H in Fig. 3c, showing that V_H is theoretically sensitive to distance z. As for the influence of other practical variables (θ, μ_r, and shear motion) on the V_H, analytical calculations (Formula 4), finite element analysis (FEA) and practical experiments are conducted to explain the full link budget between them (Fig. S21a–d). To quantify performance under magnet misalignment and lateral offset, the Hall signal variation is investigated by finite element analysis (FEA) and experiments with a neodymium magnet (25 mm diameter, 2.5 mm thickness) at a distance of 10 mm to the FSH sensor. Both of the results in Fig. S22a show that, for angular misalignments up to 15°, the signal magnitude decreases <3%. With lateral shifts of ±1 mm (corresponding to 20% of the sensing area width) from the axial site of the magnet, the maximal signal deviation is <1%, as shown in Fig. S22b. This is also validated by the simulated magnetic field in the sensing plane, which exhibits a stable value (57–58 mT) within the sensing area (Fig. S22c). Furthermore, the in vitro experiments, which mimic the tumor growing process with an inflated silicone sphere, record the real-time Hall signal shown in Fig. S23. Over 30-s expansion period, the distance from the sensor (at the top of sphere) to the magnet is reduced from 15 mm to 8 mm, while the device signal increases from 48 μV to 188 μV. The Hall voltage derived from the sensor is primarily converted into the sensor displacement based on the standard curve (Fig. S20). In the case of the FSH sensor at the top of tumor, the variation of sensor signals associated with distance between the sensor and magnet can yield information of tumor height during growth from the beginning to terminal, thus effectively capturing the tumor surface dynamics over the specified time period. This millimeter and/or micrometer

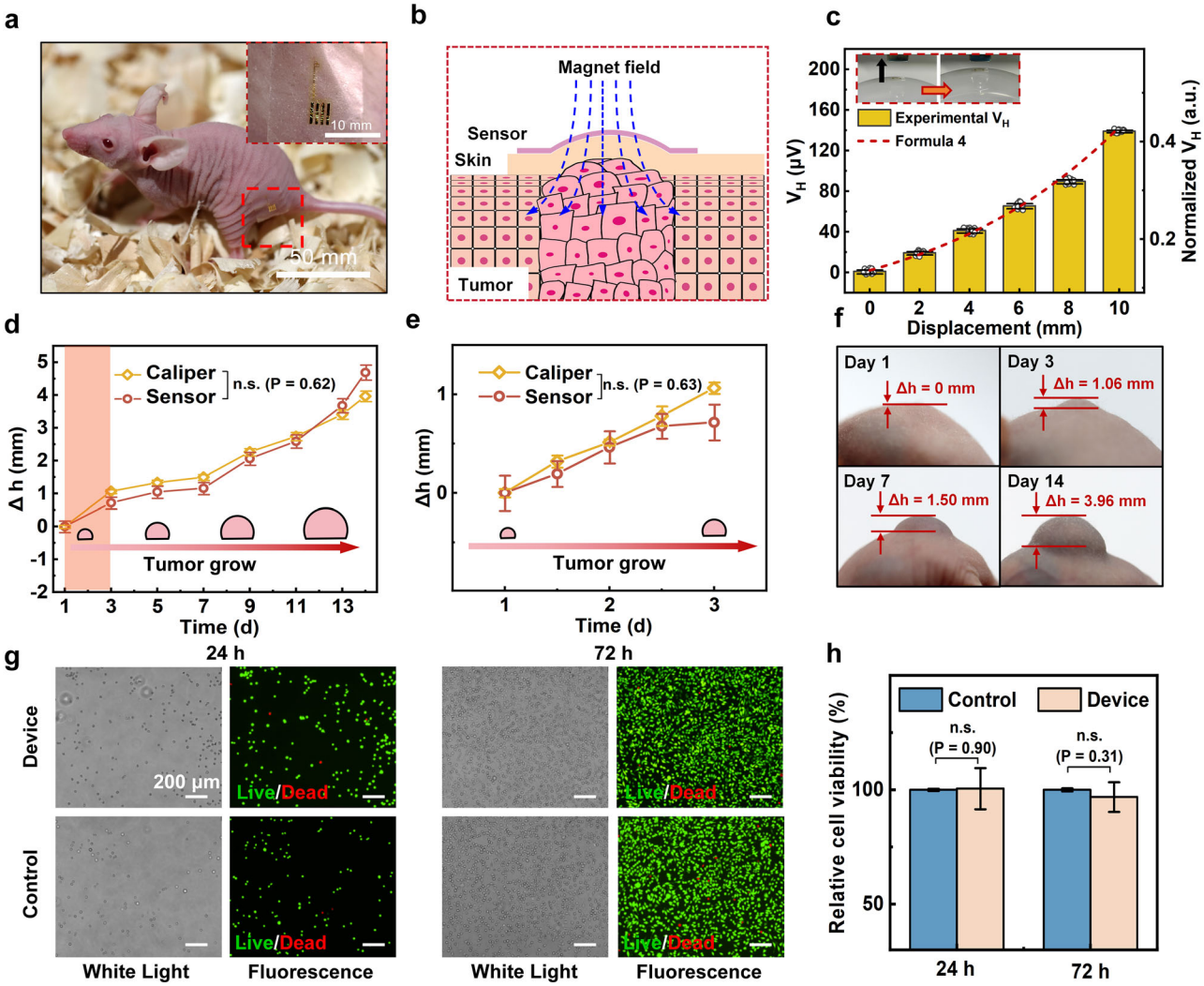

Fig. 3 | In vitro tumor growth monitoring of the FSH sensor in mouse models. **a** Optical images of the FSH sensor attached to the tumor site in mouse. The inset shows an enlarged image of the seamless attachment of the device. **b** Cross-section diagram of FSH sensor for detecting tumor height changes. **c** The variation trend of the measured Hall voltage and the theoretical magnet field as the sensor approaches the magnet on a silicone sphere. **d** Comparison of tumor height changes over 14 days measured by a caliper (yellow line) and FSH sensor (red line). **e** Early-stage tumor height monitoring of the FSH sensor during Days 1–3. **f** Side view photos of the mouse tumor on Days 1, 3, 7, and 14. **g** White light and fluorescence microscopy images of live/dead stained L929 cells co-cultured with FSH sensors (upper) as Device group and without FSH sensors (bottom) as Control group. **h** Quantitative viability assessment of Control group and Device group via cell counting Kit-8 (CCK-8) assay. Error bars represent SD ($n \geq 3$). The ns (no significance) $p > 0.05$, $^{*}p < 0.05$, $^{**}p < 0.01$, $^{***}p < 0.001$, $^{****}p < 0.0001$.

level sensing capability of FSH sensors provides a solid foundation for tumor growth monitoring.

Throughout the entire period of tumor growth in the living mouse model, the FSH sensor continuously monitors the tumor height within couples of weeks (Movie S1). As shown in Fig. 3d, the tumor height measured by the FSH sensor (orange line) over 14 days shows a noticeable increase (Δh is defined as the tumor height increment since Day 1), consistent with the result measured by the caliper tool (yellow line). Validation of the early-warning capability is further achieved through monitoring during Days 1–3 in Fig. 3e, which captures the tiny tumor height variation within 1 mm beyond the naked eye's observation, demonstrating submillimeter-scale tumor elevation dynamics surpassing the visual detection threshold. In addition, Fig. 3f presents side views of tumor in mouse on Days 1, 3, 7, and 14, with Δh increasing from 0 mm to 3.96 mm, which provide a visual illustration of tumor progression over time, allowing for a clear comparison of the growth stages and complementary validation to quantitative measurements obtained through the FSH sensor and caliper tracking methods. Additionally, to minimize the interference from the subject motion, Fig. S24a presents the schematic diagram of a custom-designed shell used to fix the magnet inside, thereby securing its distance (designed as 10 mm) relative to the underlying FSH sensor. The shell is 3D-printed using M-Silicone (MakeX, Young's modulus of 0.5 MPa), enabling stable and conformable adhesion to the skin. Figure S24b shows the integrated FSH sensor system with the shell and magnet attached to the human forearm. Upon wearing the whole FSH systems, the change in Hall voltage is neglectable during the subject's arm-swinging motion (Fig. S24c). Those results highlight the effectiveness of the FSH sensor in tracking tumor growth, with minor discrepancies that are within a rational range for practical applications.

Figure 3g presents the biocompatibility evaluation of FSH sensors through live/dead cell staining assays using mouse fibroblast cells (L929). The experimental design incorporates FSH sensor co-culture system (Device group) and sensor-free culture system (Control group) maintained under identical incubation conditions. Fluorescence microscopy imaging documents cellular responses following 24- and 72-h co-culture periods, with live cells fluorescing green and dead cells exhibiting red signals. Quantitative viability assessment via cell counting Kit-8 (CCK-8) assay reveals comparable metabolic activity between Device group (yellow) and

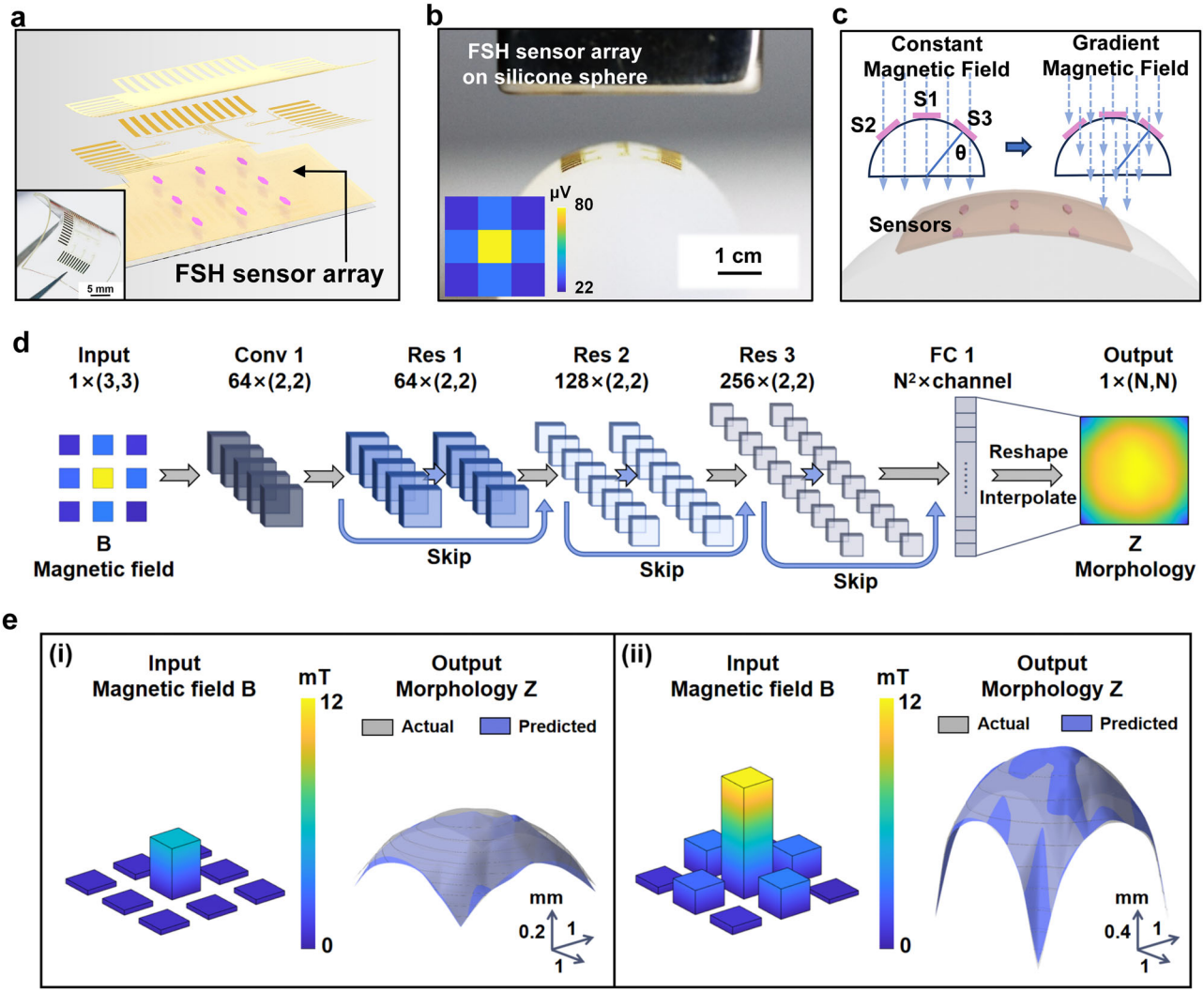

Fig. 4 | FSH sensor arrays and deep learning models for tumor dimension analysis. a Illustration and photograph (inset) of the FSH sensor array transferred onto a PDMS substrate. **b** Hall voltage signal collection of FSH sensor array attached to a 20 mm-diameter silicone sphere. Inset: The signal data mapping exhibits much stronger amplitude in the central part. **c** Calculative decoupling process of surface morphology on the spherical surface. **d** Pipeline of the residual neural network comprising input layer, convolutional layers, residual connections, fully connected layers and output layer. Here, $N = 7$ is the optimal result. **e** Two representative examples of tumor morphology reconstruction images sampled from the dataset: (i) Small curvature surface and (ii) Large curvature surface.

Control group (blue) across 72 h (Figs. 3h and S25). Statistical analysis confirms no statistically significant reduction in relative cell viability. To validate the long-term biocompatibility, the histological analyses after 2 weeks of continuous attachment to the dorsal skin tissue of mice are supplemented. The Hematoxylin–Eosin (H&E) staining results of the skin tissue (Fig. S26a) reveal no signs of epidermal disruption, erythema, edema, or inflammatory cell infiltration beneath the contact area in the Device Group. The skin structure, including the stratum corneum and epidermal thickness, remains comparable to that of the Control Group. The Masson's Trichrome staining results in Fig. S26b show no noticeable increase in collagen fiber density or dermal fibrosis under the FSH sensor attachment region, indicating that prolonged wear does not induce chronic skin irritation. These findings validate the biological stability and safety of the FSH sensor in physiological environments, establishing a critical foundation for its extended biocompatible operation in prolonged diagnostic/therapeutic applications.

FSH sensor arrays and deep learning models for tumor dimension analysis

Beyond the individual FSH sensor, a multi-sensor array of FSH can achieve high-resolution spatiotemporal mapping across tumor surface topography, yielding clinical significance for guiding subsequent treatment strategies in practice, particularly in cases where the tumor is malignant or morphologically altered. Such information about tumor progression, such as the shape and volume, relies on three-dimensional (3D) tumor morphology reconstruction by use of sensor array configuration. Figure 4a displays the illustration and the optical image (inset) of the FSH sensor array on the PDMS substrate (500 μm thick), while Fig. S27 shows the circuit layout. Specifically, the entire array consists of 9 FSH sensors (3 columns, 3 rows), each with dimensions of 300 μm by 100 μm, distributed uniformly over a total area of $5 \times 5\ mm^2$. Each FSH sensor in nanomembrane forms (200 nm) incorporates two metal electrodes that enable the capability of addressing for tumor surface geometrics mapping. The fabrication details appear in "Methods" section. The total thickness of the FSH sensor array is less than 20 μm, thus yielding exceptional flexibility and conformability (Fig. S28).

To further illustrates morphology detecting functionality, the sensor array forms conformal contact with the curving surface of a 20 mm-diameter silicone sphere to simulate the attachment on in vitro tumor, with a permanent magnet located 20 mm above to generate a gradient magnetic field in Fig. 4b. The inset presents the mapping of Hall voltage signal extracted from the FSH sensor array, where the central sensor exhibits the strongest signal and the corner sensors display the much weaker signal.

This distribution is attributed to the magnetic flux variation across each sensor, which is determined by both the distance and angle between the sensor and the magnet, with the FEA analysis in Fig. S29. Therefore, to decouple the exact distance and angle value from the Hall voltage signal to reconstruct the surface morphology is of great importance. Figure 4c exhibits an operation approach by variables separation to realize the decoupling process. Specifically, the first step is to place the array in the constant magnetic field with unchangeable magnetic field intensity, thereby the angle θ (defined as the angle between the magnetic vector and the normal vector of the sensor plane) can be calculated from the Hall voltage intensity. Then, the second step is to place the array in the gradient magnetic field. Because of the known angle value of each sensor, the Hall voltage only depends on the magnetic intensity at the site of the sensor, from which the distance can be inferred via Formula 3. Detailed calculation processes appear in Fig. S30.

Furthermore, to avoid the complex calculations during the decoupling process, the deep learning models are proposed to perform the tumor dimension analysis via magnetic field distribution, which is converted from the Hall voltage mapping by Formula 1. A convolutional neural network (CNN) involving a single convolutional (Conv) layer and a fully connected (FC) layer is already established to obtain the tumor height and volume (Fig. S31), yet still facing challenges such as vanishing gradients related to the difficulty of information propagation and limited generalization capability when attempting morphology reconstruction[66]. To maximize the retention of local gradient information[67], the residual neural network (ResNN) in Fig. 4d is employed, which consists of a convolutional (Conv) layer, three residual (Res) layers, and a fully connected (FC) layer. Here, the input layer is the magnetic field mapping data in size of (3, 3) and the kernel size for Conv/Res layer is (2, 2). Each Res layer involves two convolutional layers and introduces residual connections through skips, allowing gradients to be directly propagated through, thus effectively avoiding the vanishing gradient problem and enhancing the generalization capability of the model. Instance batch normalization and Leaky ReLU activation are used for each layer. The output features of the last Res layer are directly transferred to the FC layer for the regression task, where the number ($N^2 = 49$) of output channels is the optimized result, followed by reshaping and interpolation to form the output morphology matrix data in size of (N, N) ($N = 7$). The investigation about the output channel number (Fig. S32) shows that as N increases from 3 to 7, the average Mean Square Error (MSE) between the predicted and validated morphology data in the entire dataset decreases from 0.016 to 0.009, while the average correlation coefficient (r) increases from 0.83 to 0.91. However, as N increases more than 7, massive network architectures and intricate data preprocessing procedures lead to the excessive computational time and cost for our practical measurement, establishing (7, 7) as the optimal output matrix configuration.

To enhance the stability of model evaluation and maximize the utilization of data[62], K-fold cross-validation (KF-CV, $K = 5$) tests are employed with randomly mixed datasets, as shown in Fig. S33. The datasets are randomly divided into five parts, with each part performed as the validation set in turn, while the remaining four parts serve as the training set. After completing the five iterations, the validation loss function value (refers to MSE) of the five folds ranges from 0.013 to 0.068, with the average value obtained as 0.039. As a comparison, this performance is significantly better than those of CNN and ResNN without K-fold cross-validation, with validation loss function value of 0.104 and 0.085, respectively (Fig. S34), which demonstrates the superiority of the model in morphology data reconstruction. Furthermore, Fig. 4e presents two representative examples of tumor morphology reconstruction results, including conditions of (1) small curvature surface and (2) large curvature surface. In both cases, the predicted 3D surface (blue) exhibits a high degree of consistency with the actual 3D surface (gray), demonstrating the practicality and stability of the residual neural network with K-fold cross-validation in surface profile reconstruction. Notably, the same deep learning models, including CNN and ResNN, can be extended to larger sensor arrays to obtain geometrical parameters and achieve large-scale topography restoration.

Real-time monitoring of the FSH sensor arrays for tumor development in animal models

To validate the practical utility of the combination of the FSH sensor array and deep learning models, the mouse tumor model transplanted with SK-N-BE(2) cells is employed (Fig. S35). Here, the CNN is used for critical geometrical parameter extraction (i.e., height and volume) while the ResNN is three-dimensional tumor profile reconstruction. Comprehensive tumor growth analysis is performed at the four key time points (Days 1, 3, 7, and 14), where Fig. 5a illustrates serial whole-body images showing progressive tumor development. Notably, the tumor exhibits three-dimensional expansion along multiple axes, maintaining an approximately spheroidal configuration while developing increasingly intricate surface morphological features over the observation period. Figure 5b corresponds to the associated computed tomography (CT) images during the tumor growth at the four stages, consistent with those of Fig. 5a. These longitudinal observations reveal a strong correlation between tumor growth dynamics and morphological variations, demonstrating two notable characteristics: continuous volumetric expansion accompanied by progressive acceleration in growth rate and multidirectional proliferation patterns resembling spherical inflation with increasing structural complexity.

As a comparison, Fig. 5c presents the four-stage tumor profile reconstruction achieved through the ResNN discussed in Fig. 4d, where the testing scheme appears in Fig. S36. Detailed information is in "Methods". Results show the precise 3D profile during early tumor development within a week, and effectively capture both volumetric expansion and surface irregularity patterns, in an agreement to the above optical and CT images in Fig. 5a, b. As the tumor height exceeds 5 mm (Day 14), the reconstructions exhibit partial volume loss and boundary discontinuities, thus failing to provide the entire tumor shape, due to the limitation of the effective sensing area as 5×5 mm^2 of the FSH array. To further address the spatial coverage limitation, the array design can be scaled up by multi-transfer printing of Si-NMs[68] to achieve high-channel-count FSH array. This strategy can extend both lateral and vertical measurement ranges to accommodate larger tumor volumes in future works. Furthermore, to validate the dynamic monitoring reliability of the arrayed FSH sensor together with CNN in tumor dimension quantitative assessment, the comparative results of the tumor height and volume derived through CT, caliper and neural network are presented in Fig. 5d. Here, the neural network is trained repeatedly for one hundred times, and the output height and volume are recorded after each training. These comprehensive quantitative analysis of multiple parameters of tumors reveal strong correlations, demonstrating the temporal alignment across four characteristic growth stages (Day 1, 3, 7, and 14). In addition, to further investigate the agreement between the predicted tumor dimensions and the measured tumor dimensions (defined as the average of CT and caliper results), the statistical analysis is performed to reveal that the mean differences and standard deviations in tumor height and volume between measured result (H_{Mea}, V_{Mea}) and predicted result (H_{Mea}, V_{Mea}) are 0.004 ± 0.089 mm and -0.35 ± 10.37 mm^3, respectively, indicating that the deep learning-assisted FSH sensor arrays are able to obtain reliable tumor geometric parameters with exceptional robustness and generalization. Additionally, Table S3 summarizes optical methods (including caliper measurement, micro-CT, photoacoustic imaging and optoelectronics), strain-based methods, and Hall-based methods (this work), in terms of their working principles, minimum detectable tumor size, detection precision, environmental tolerance, monitoring duration, and limitations. The comparison reveals that the FSH sensor features the capabilities of direct quantification of tumor volume, robust operation under opaque, low-light, and motion conditions, and continuous, non-invasive monitoring on skin surfaces.

Furthermore, such an FSH sensor array shows the potential in wireless, remote monitoring capability by use of the analog circuit

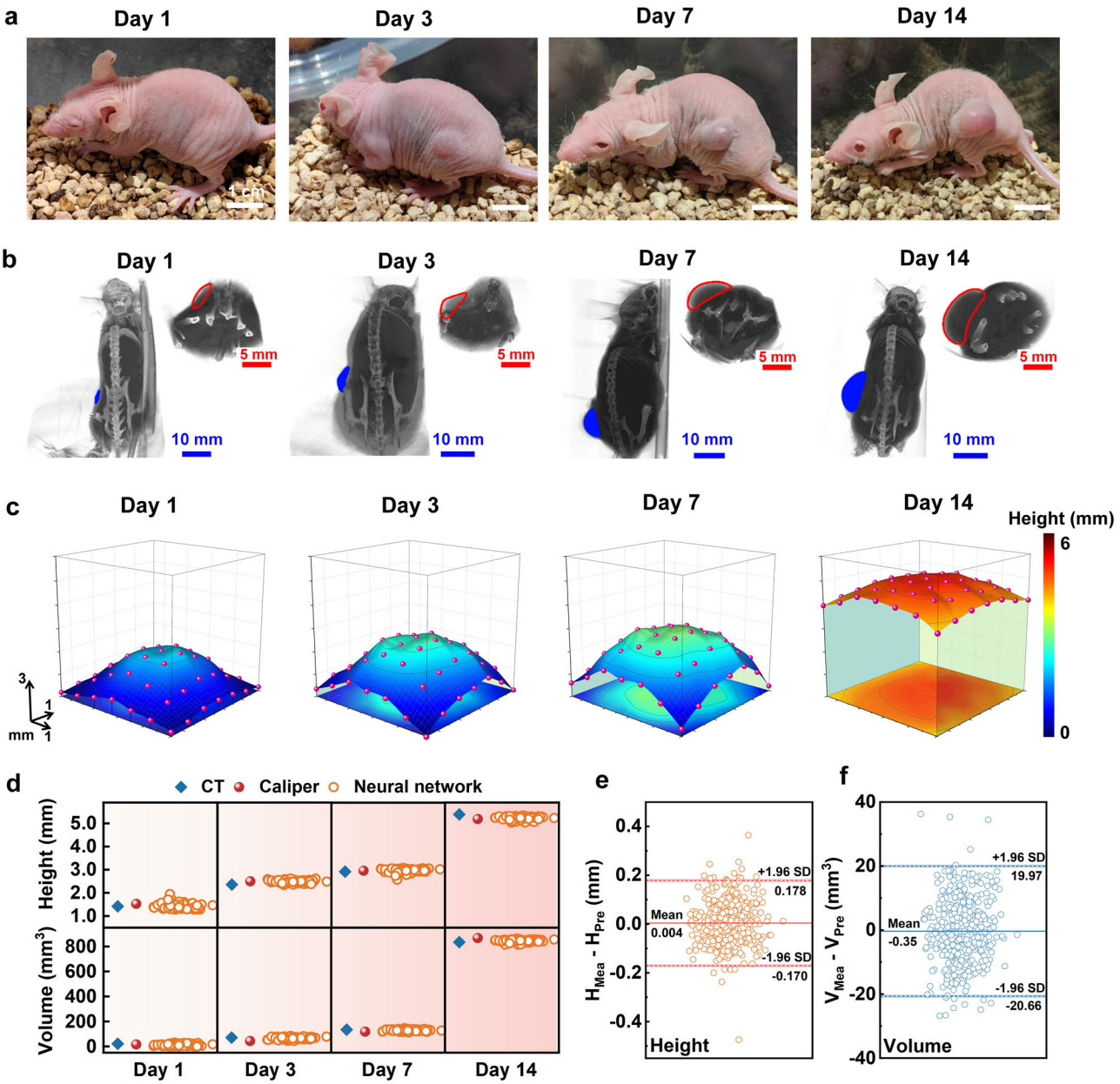

Fig. 5 | In vivo tumor morphology reconstruction of the FSH sensor array in mouse model. a Photographs of the tumors grown on the left side of the mouse over 14 days. **b** The in situ tumor CT results of the mouse on Days 1, 3, 7, and 14. **c** Reconstruction results of the tumor on Days 1, 3, 7, and 14 through the deep learning model. **d** The comparative results of the tumor height and volume from CT, caliper, and sensors with neural network. **e** The differences between the measured tumor height (H_{Mea}) and the predicted tumor height (H_{Pre}) through the neural network. **f** The differences between the measured tumor volume (V_{Mea}) and the predicted tumor volume (V_{Pre}) through the neural network. Here, SD stands for standard deviation, and the Mean ± 1.96 SD stands for limits of agreement.

design and Bluetooth program construction (Fig. S37). Specifically, the system uses an ARM Cortex-M4 CPU-based Bluetooth Low Energy (BLE) System-on-Chip (nRF52832) as the microcontroller. The constant current source LM234DT provides a configurable operating current for the Hall device, while the multiplexers 74HC4067BQ and CH448F enable address-selected measurements within the array. Figure S38a, b shows the circuit schematic diagram and the PCB layout. The overall system-level circuit module measures 4.7 cm in length and 3.6 cm in width, with a thickness less than 2 mm (Fig. S38c). The supply current profiles in Fig. S38d reveal the power consumption of the analog front-end (AFE) and Bluetooth Low Energy (BLE) transceiver. In standby and transmission period, the whole system features the quiescent current at hundreds of microampere level, while the dynamic BLE spike current is more than 2 mA. In the detection period, the system consumes the average working current of 1.3 mA (including 1 mA for FSH sensors) during continuous data sampling/processing /transmission at 0.5 Hz. The calculated power consumption is 0.55 mW, 4.28 mW and 0.96 mW during the standby, detection and transmission mode (Fig. S38e). Using a 100 mAh/3.7 V lithium-polymer battery (as shown in Fig. S38f), the estimated continuous operating time is 20 days, assuming a duty-cycled scheme (5% detection, 5% transmission, and 90% standby). Figure S38g shows that the received signal strength indicator (RSSI) ranges from −31 dBm to −62 dBm with the transmission distance increasing to 2.5 m, enabling the effective data rate of 217 kbps to 148 kbps for a 3 × 3 FSH sensor array (equal to 753–513 Hz sampling frequency per channel), which confirms robust wireless communication under typical laboratory and in vivo conditions.

Discussion

In conclusion, this study demonstrates the applicable development of a flexible, wearable Hall sensor array for high-precision monitoring of tumor growth dynamics through magnetic flux variation. By integrating ultrathin silicon nanomembranes (Si-NMs) as functional elements, the device achieves exceptional sensitivity (4.41 V/A T) and 1 μT detection limit, enabling microscale resolution in capturing dimension changes during early-stage tumor progression. The conformal design ensures reliable adhesion to biological surfaces, as validated through in vivo experiments on mouse models under gradient magnetic fields to continuously track tumor height variations. The synergistic combination of arrayed sensor architecture and deep learning frameworks, particularly convolutional and residual neural networks, advances the capability for volumetric quantification, overcoming traditional limitations in large-area, three-dimensional tumor profiling. Importantly, while our device does not aim to replace large-scale imaging systems such as CT or PAI, it achieves higher sensitivity for smaller, early-stage tumors that are difficult to be detected by conventional manual or imaging methods, thereby filling a critical gap between wearable sensing and medical imaging. The scalability of the platform, coupled with its compatibility with machine learning algorithms, suggests broader applications in precision oncology and personalized medicine. Future work will focus on clinical translation through multi-parameter correlation with histological data, user-friendly operation interface, and integration with closed-loop therapeutic systems. These innovations collectively represent a significant step toward dynamic, data-driven approaches in cancer management, bridging critical gaps between laboratory research and clinical.

Methods

Fabrication of the FSH sensor and the array

The cleaned SOI (220 nm Si/1 μm SiO_2; SOITEC) are doped in a tube furnace (960 °C 15 min, N2: 1 L/min; 1200 °C 30 min) to obtain a boron concentration of ~10^{19} atoms/cm^3. The surface oxide layer formed in the doping process of the doped SOI wafer is removed by buffered oxide etchant (BOE) solution. Micropores (4 μm diameter/40 μm pitch) are formed on the device layer by lithography (MA6, SUSS), photoresist S1805 (~ 1 μm, 3000 rpm 30 s, Dow), and reactive ion etching (RIE, T2, Trion). PMMA (950 PMMA A7, ~1 μm; MicroChem) and PI (~ 5 μm; Changzhou Yaan new materials Co., LTD) are spin-coated on a cleaned glass wafer (15 × 15 mm^2) as the sacrificial layer and the substrate layer of the device, respectively. The PMMA is cured at 180 °C for 90 s, and PI layer is then pre-cured at 110 °C for 2 min.

Buried oxide layer of the pre-prepared doped SOI is etched in HF solution (49%) for ~45 min to release the device layer. Picking up the device layer with a PDMS stamp (base: curing agent = 4:1) and pressing the stamp on the receiver substrate to transfer the device layer from the doped SOI to the PI substrate. The PI substrate after transfer printing of Si-NM is completely cured at 250 °C for 2 h. The Si-NM with topological structure or the array configuration is defined by lithography and RIE etching. The electrode connections of the sensor consist of Cr/Au films (10/100 nm) prepared by magnetron sputtering (DE500, DE Technology), and the wiring patterning of the metal is determined by lithography and wet etching. The sensor is finally encapsulated by another layer of PI (~ 5 μm). The excess encapsulation material on the opening window of the electrodes is removed by lithography and RIE etching. The sample is subsequently immersed in acetone (~13 h) to dissolve the PMMA sacrifice layer and release the device from the glass wafer. The fabrication process is completed by transferring the device from the glass wafer to the PDMS (~ 30 μm) flexible substrate through a WST (3 M 5414 TRANSPARENT).

FEA simulation

To more effectively design a high-sensitivity Si-NM shape, COMSOL Multiphysics® is used to perform FEA simulations and validates the results through experiments. We adjusted the size, aspect ratio of the Si-NM, taper angle and the contact area of the electrodes to design the Si-NR dimensions and electrodes. The results indicate that the size of the Si-NM does not affect the sensitivity of sensor, and the signal saturates at an aspect ratio of 1:3. Additionally, the highest sensitivity is achieved when the contact areas of source and drain electrodes occupy nearly the half while the contact area of the Hall electrodes is minimized.

In addition, COMSOL Multiphysics® is further used to validate the robustness of the flexible devices, especially the Si-NM part. The device layers, including Si-NM, metal, PI and PDMS, with the Young's modulus of 170 GPa, 70 GPa, 3.1 GPa, and 750 KPa respectively, are united in the Solid Mechanics field. Stretching, bending, and twisting tests have been performed with a Static analysis step.

Characterization the Si-NM-based FSH sensor

For alternative magnetic field, the signal for the electromagnetic coil and the bias current/voltage for the FSH sensor are provided by the waveform generator (Keysight 33500B) and the source meter (Keysight B2902B), respectively. Different magnetic fields are generated by adjusting the amplitude and frequency of the signal generator. For non-alternative magnetic field, the permanent magnet is used and the bias current/voltage for the FSH sensor are provided by the waveform generator (Keysight 33500B). The Hall voltage signal induced by the magnetic field is extracted using a lock-in amplifier (Stanford Research Systems Model SR830 DSP).

In vitro experiment

For better adherence to the skin, the FSH sensor is first transferred onto a highly adhesive PDMS substrate. PDMS substrates are prepared by the template method, where the mold is a 200 μm thick silicone film. The PDMS is mixed with a ratio of 20:1, followed by pouring into the mold and cured at 80 °C for 12 h. When attached to a fingernail to monitor the geomagnetic field, the signal has to be calibrated in a zero-Tesla chamber. The geomagnetic field monitoring is performed in an open environment free from interference by other magnetic fields. During the experiment, the device is rotated by turning the finger. For displacement monitoring, the signal from the initial position is used as the baseline for calibration. The signal changes induced by the displacement of the FSH sensor are then monitored to accurately detect the displacement of the attached target.

In vivo tumor monitoring experiment

The animal studies employ 6–7-week-old female athymic nude mouse (BALB/C-NU/+, $N = 3$), living with a 12-h light/dark cycle with a temperature-controlled (24 °C) animal facility. SK-N-BE(2) cells (Cell Bank of the Chinese Academy of Sciences) are resuspended in PBS and counted (50 μL of the cell suspension with 50 μL of a 0.2% trypan blue staining solution, followed by quantification using an automated hemocytometer). A mixture of 10^6 SK-N-BE(2) neuroblastoma cells suspended in 50 μL of PBS along with 50 μL of Matrigel basement membrane matrix (Leyou Biotech). Under isoflurane anesthesia, the mixture is draw up 100 μL by 1 mL syringe and injected subcutaneously into the left flank of each mouse. Tumor growth is monitored on the following days using FSH sensors, calipers, and CT imaging. Within each animal, at every time point, we perform three consecutive repeated measurements as technical replicates. Before each FSH monitoring session, the mice are anesthetized with isoflurane, secured on the operating platform, and the distance between the restraint device and the magnet is maintained constant. The Hall voltage values of each unit in the array are then recorded. For CT imaging, the mice are similarly anesthetized with isoflurane, and a Micro-CT system (SkyScan 1276) is utilized. The humane endpoint is defined as tumor size greater than 2 cm in its largest dimension or 2000 mm^3 in volume. Mice are subjected to confirmatory cervical dislocation within 12 h of reaching the humane endpoint. Two-way ANOVA is performed to quantify the statistical difference of the results.

Deep learning neural networks

The deep learning model is trained using Python 3, with a dataset comprising 400 sets of COMSOL-simulated magnetic field distributions on tumor surfaces under gradient magnetic fields, along with

tumor height, volume, and 3D morphology data. Data preprocessing involves converting magnetic field distribution information into 3×3 2D arrays followed by standardization before feeding them into the neural network. A convolutional neural network (CNN) is used to predict tumor height and volume, while a residual neural network (ResNet) architecture is employed for morphology prediction, as detailed in the main text. The CNN outputs tumor height and volume, whereas the ResNet generates a 7×7 2D morphology array. Training utilize the TensorFlow framework with the Adam optimizer and accelerated using an NVIDIA RTX 4060 GPU.

Cytotoxicity evaluation

The Si-NM-based FSH sensor is sterilized by UV irradiation and co-cultured with L929 cells (Procell Life Science & Technology Co., Ltd.) for 24 h and 72 h in a constant temperature incubator (37 °C). Cultured cells are stained using the Calcein-AM/PI double-stain kit (BB-4126, BestBio) and incubated for 15 min at 25 °C. Fluorescence microscopy is used to obtain the images of stained live and dead cells. The co-cultured cells are added to the culture medium containing 10% CCK-8 (IV08-100, Invigentech) and incubated at 37 °C for 2 h to evaluate the relative cell viability. Relative cell viability is reflected by measuring the absorbance value at 450 nm using a microplate reader.

Statistical analysis

All data are expressed as mean ± standard deviation (SD) unless otherwise stated. Statistical differences between two independent groups are analyzed using an Independent-Sample *T*-test, while datasets involving two experimental factors are evaluated using two-way ANOVA. A p value < 0.05 is considered statistically significant. The number of samples (n) for each dataset is indicated in the corresponding figure captions. Error bars in all graphs represent standard deviations. All statistical analyses are performed using Origin 2021.

Ethics approval

All animal studies were approved by the Animal Welfare and Research Ethics Committee at Fudan University (ID: 2023-GGWS-17JZS). For contents regarding experiments with human subjects (illustrative photos of sensors attaching to the human skin), approval was obtained from the Ethics Committee of Zhongshan Hospital, Fudan University (ID: Y2021073). The informed consent was obtained from all participants involved in this entire study.

Data availability

All data are available in the main text or the Supplementary Materials. All data needed to evaluate the conclusions in the paper are present in the paper and/or the Supplementary Materials.

Received: 28 August 2025; Accepted: 10 December 2025;
Published online: 27 December 2025

References

1. Chen, H., Zhang, W., Zhu, G., Xie, J. & Chen, X. Rethinking cancer nanotheranostics. *Nat. Rev. Mater.* **2**, 17024 (2017).
2. Mi, P. et al. A pH-activatable nanoparticle with signal-amplification capabilities for non-invasive imaging of tumor malignancy. *Nat. Nanotech.* **11**, 724–730 (2016).
3. Coombes, R. C. et al. Personalized detection of circulating tumor DNA antedates breast cancer metastatic recurrence. *Clin. Cancer Res.* **25**, 4255–4263 (2019).
4. Moding, E. J., Nabet, B. Y., Alizadeh, A. A. & Diehn, M. Detecting liquid remnants of solid tumors: circulating tumor DNA minimal residual disease. *Cancer Discov.* **11**, 2968–2986 (2021).
5. Davis, L. E., Shalin, S. C. & Tackett, A. J. Current state of melanoma diagnosis and treatment. *Cancer Biol. Ther.* **20**, 1366–1379 (2019).
6. Folkman, J. Tumor angiogenesis: therapeutic implications. *N. Engl. J. Med.* **285**, 1182–1186 (1971).
7. Friberg, S. & Mattson, S. On the growth rates of human malignant tumors: implications for medical decision making. *J. Surg. Oncol.* **65**, 284–297 (1997).
8. Ortmann, J. et al. Assessing therapy response in patient-derived xenografts. *Sci. Transl. Med.* **13**, eabf4969 (2021).
9. Enderling, H. & Chaplain, H. E. M. Mathematical modeling of tumor growth and treatment. *Curr. Pharm. Des.* **20**, 4934–4940 (2014).
10. Song, E. et al. Miniaturized electromechanical devices for the characterization of the biomechanics of deep tissue. *Nat. Biomed. Eng.* **5**, 759–771 (2021).
11. Zheng, Y. & Mak, A. F. T. Effective elastic properties for lower limb soft tissues from manual indentation experiment. *IEEE Trans. Rehabil. Eng.* **7**, 257–267 (1999).
12. Gennisson, J.-L. et al. Assessment of elastic parameters of human skin using dynamic elastography. *IEEE Trans. Ultrason. Ferroelectr. Freq. Control.* **51**, 980–989 (2004).
13. Zhang, W. et al. Real-time, volumetric imaging of radiation dose delivery deep into the liver during cancer treatment. *Nat. Biotechnol.* **41**, 1160–1167 (2023).
14. Prasad, S. R. et al. CT tumor measurement for therapeutic response assessment: comparison of unidimensional, bidimensional, and volumetric techniques—initial observations. *Radiology* **225**, 416–419 (2002).
15. Taylor, F. G. M. et al. Preoperative magnetic resonance imaging assessment of circumferential resection margin predicts disease-free survival and local recurrence: 5-year follow-up results of the mercury study. *J. Clin. Oncol.* **32**, 34–43 (2014).
16. Mann, R. M. N. & Moy, C. L. Breast MRI: state of the art. *Radiology* **292**, 520–536 (2019).
17. Saini, S. Multi–detector row CT: principles and practice for abdominal applications. *Radiology* **233**, 323–327 (2004).
18. Hu, J. & Soleimani, M. Combining multiple boundary shapes in deformable EIT a potential use in breast imaging. *IEEE Sens. Lett.* **4**, 1–4 (2020).
19. Doucey, M.-A. & Carrara, S. Nanowire sensors in cancer. *Trends. Biotechnol.* **37**, 86–99 (2019).
20. Elaibi, H. K., Mutlag, F. F., Halvaci, E., Aygun, A. & Sen, F. Review: Comparison of traditional and modern diagnostic methods in breast cancer. *Measurement* **242**, 116258 (2025).
21. Hu, S. et al. An electrode array sensor for tongue cancer detection with bioelectrical impedance spectroscopic tomography. *IEEE Sens. J.* **22**, 15146–15153 (2022).
22. Wang, L. et al. Functionalized helical fibre bundles of carbon nanotubes as electrochemical sensors for long-term in vivo monitoring of multiple disease biomarkers. *Nat. Biomed. Eng.* **4**, 159–171 (2019).
23. Kim, K. et al. Fully implantable and battery-free wireless optoelectronic system for modulable cancer therapy and real-time monitoring. *npj Flex. Electron.* **7**, 41 (2023).
24. Siboro, P. Y. et al. Harnessing HfO_2 nanoparticles for wearable tumor monitoring and sonodynamic therapy in advancing cancer care. *ACS Nano*. **18**, 2485–2499 (2024).
25. Abramson, A. et al. A flexible electronic strain sensor for the real-time monitoring of tumor regression. *Sci. Adv.* **8**, eabn6550 (2022).
26. Geng, S. et al. Ultrasensitive optical detection and elimination of residual microtumors with a postoperative implantable hydrogel sensor for preventing cancer recurrence. *Adv. Mater.* **36**, 2307923 (2024).
27. Lee, C.-Y., Lin, Y.-Y., Kuo, C.-K. & Fu, L.-M. Design and application of mems-based hall sensor array for magnetic field mapping. *Micromachines* **12**, 299 (2021).
28. Li, R. et al. A spin–orbit torque device for sensing three-dimensional magnetic fields. *Nat. Electron.* **4**, 179–184 (2021).

29. Zieren, V. A new silicon micro-transducer for the measurement of the magnitude and direction of a magnetic-field vector. *Paper Presented at the 1980 International Electron Devices Meeting, IEEE, Washington, USA*, 8 (1980).
30. Heremans, J. Solid-state magnetic-field sensors and applications. *J. Phys. D Appl. Phys.* **26**, 1149–1168 (1993).
31. Hu, H. et al. Large-area magnetic skin for multi-point and multi-scale tactile sensing with super-resolution. *npj Flex. Electron.* **8**, 42 (2024).
32. Wan, J. et al. Millimeter-scale magnetic implants paired with a fully integrated wearable device for wireless biophysical and biochemical sensing. *Sci. Adv.* **10**, eadm9314 (2024).
33. Mostufa, S., Yari, P., Rezaei, B., Xu, K. & Wu, K. Flexible magnetic field nanosensors for wearable electronics: a review. *ACS Appl. Nano Mater.* **6**, 13732–13765 (2023).
34. Hu, H. et al. Wireless flexible magnetic tactile sensor with super-resolution in large-areas. *ACS Nano*. **16**, 19271–19280 (2022).
35. Pan, L. et al. Flexible magnetic sensors. *Sensors* **23**, 4083 (2023).
36. Melzer, M. et al. Wearable magnetic field sensors for flexible electronics. *Adv. Mater.* **27**, 1274–1280 (2014).
37. Cañón et al. Electronic-skin compasses for geomagnetic field-driven artificial magnetoreception and interactive electronics. *Nat. Electron.* **1**, 589–595 (2018).
38. Oliveros-Mata, E. S. et al. Dispenser printed bismuth-based magnetic field sensors with non-saturating large magnetoresistance for touchless interactive surfaces. *Adv. Mater. Technol.* **7**, 2200227 (2022).
39. Wang, X. et al. Physical investigations on bias-free, photo-induced hall sensors based on Pt/GaAs and Pt/Si schottky junctions. *Sensors* **21**, 3009 (2021).
40. Berus, T., Oszwaldowski, M. & Grabowski, J. High quality Hall sensors made of heavily doped n-InSb epitaxial films. *Sens. Actuators A Phys.* **116**, 75–78 (2004).
41. Kaidarova, B. A. et al. Flexible Hall sensor made of laser-scribed graphene. *npj Flex. Electron.* **5**, 2 (2021).
42. Wang, Z., Shaygan, M., Otto, M., Schall, D. & Neumaier, D. Flexible Hall sensors based on graphene. *Nanoscale* **8**, 7683–7687 (2016).
43. Uzlu, B. et al. Gate-tunable graphene-based Hall sensors on flexible substrates with increased sensitivity. *Sci. Rep.* **9**, 18059 (2019).
44. Shah, N. et al. Highly stable integration of graphene Hall sensors on a microfluidic platform for magnetic sensing in whole blood. *Microsyst. Nanoeng.* **9**, 71 (2023).
45. Heidari, H., Bonizzoni, E., Gatti, U., Maloberti, F. & Dahiya, R. CMOS vertical Hall magnetic sensors on flexible substrate. *IEEE Sens. J.* **16**, 8736–8743 (2016).
46. Lozanova, S., Noykov, S. & Roumenin, C. Two-axis silicon Hall effect magnetometer. *Sens. Actuators A Phys.* **267**, 177–181 (2017).
47. Granell, P. N. et al. Highly compliant planar Hall effect sensor with sub 200 nT sensitivity. *npj Flex. Electron.* **3**, 3 (2019).
48. Schaefer, B. T. et al. Magnetic field detection limits for ultraclean graphene Hall sensors. *Nat. Commun.* **11**, 4163 (2020).
49. Guo, Z. et al. Geometry optimization of planar hall devices under voltage biasing. *IEEE Trans. Electron Devices.* **61**, 4216–4223 (2014).
50. Lozanova, S., Ivanov, A. & Roumenin, C. Hall sensor with geometry-enhanced sensitivity. *Paper Ppresented at the 2020 XXX International Scientific Symposium 'Metrology and Metrology Assurance' (MMA 2020), IEEE, Sozopol, Bulgaria* (2020).
51. Jiang, Z. et al. A 1.3-micrometre-thick elastic conductor for seamless on-skin and implantable sensors. *Nat. Electron.* **5**, 784–793 (2022).
52. Xu, L. et al. 3D multifunctional integumentary membranes for spatiotemporal cardiac measurements and stimulation across the entire epicardium. *Nat. Commun.* **5**, 3329 (2014).
53. Son, D. et al. Multifunctional wearable devices for diagnosis and therapy of movement disorders. *Nat. Nanotech.* **9**, 397–404 (2014).
54. Hu, B. et al. Ultrathin crystalline silicon–based omnidirectional strain gauges for implantable/wearable characterization of soft tissue biomechanics. *Sci. Adv*. **10**, eadp8804 (2024).
55. Hassan, A. et al. A DC to 25 MHz current sensing interface for Hall-effect sensor. *IEEE Sens. J.* **24**, 10316–10325 (2024).
56. Rogers, J. A. et al. Synthesis, assembly and applications of semiconductor nanomembranes. *Nature* **477**, 47–53 (2011).
57. Bal, M., Deng, C., Orgiazzi, J. L., Ong, F. R. & Lupascu, A. Ultrasensitive magnetic field detection using a single artificial atom. *Nat. Commun.* **3**, 1324 (2012).
58. Wang, Y. J. et al. A review on equivalent magnetic noise of magnetoelectric laminate sensors. *Philos. Trans. R. Soc. A Math. Phys. Eng. Sci.* **372**, 20120455 (2014).
59. Vervaeke, K., Simoen, E., Borghs, G. & Moshchalkov, V. V. Size dependence of microscopic Hall sensor detection limits. *Rev. Sci. Instrum.* **80**, 074701 (2009).
60. Kim, D. H. et al. Materials and noncoplanar mesh designs for integrated circuits with linear elastic responses to extreme mechanical deformations. *Proc. Natl. Acad. Sci. USA* **109**, 19910–19915 (2012).
61. Kim, J. et al. Stretchable silicon nanoribbon electronics for skin prosthesis. *Nat. Commun.* **5**, 5747 (2014).
62. Kim, T. et al. Ultrathin crystalline-silicon-based strain gauges with deep learning algorithms for silent speech interfaces. *Nat. Commun.* **13**, 5815 (2022).
63. Jackson, J. D. *Classical Electrodynamics* 184–188 (Wiley, 1998).
64. Furlani, E. P. *Permanent Magnet and Electromechanical Devices: Materials, Analysis, and Applications* 126–130 (Academic Press, 2001).
65. Ravaud, R. et al. Cylindrical magnets and coils: fields, forces, and inductances. *IEEE Trans. Magn.* **46**, 3585–3590 (2010).
66. Bengio, Y., Simard, P. & Frasconi, P. Learning long-term dependencies with gradient descent is difficult. *IEEE Trans. Neural Networks* **5**, 157–166 (1994).
67. He, K., Zhang, X., Ren, S. & Sun, J. Deep residual learning for image recognition. *Paper Presented at the 2016 IEEE Conference on Computer Vision and Pattern Recognition (CVPR), IEEE, Las Vegas, USA* (2016).
68. Song, E. et al. Flexible electronic/optoelectronic microsystems with scalable designs for chronic biointegration. *Proc. Natl. Acad. Sci. USA* **116**, 15398–15406 (2019).

Acknowledgements

This work is supported by the STI 2030-Major Project (2022ZD0209900), the National Natural Science Foundation of China (62204057, 62574057, T25B2012, 62304044, 82304124, 12425204, 12372096), Lingang Laboratory (LGL-8998-09), Science and Technology Commission of Shanghai Municipality (22ZR1406400), State Key Laboratory of Integrated Chips and Systems (SKLICS-Z202306), National Key R&D Program of China (2022YFB3204800), CAS Project for Young Scientists in Basic Research (YSBR-081), and Strategic Priority Research Program of the Chinese Academy of Sciences (XDB0670000). We also appreciate the support from Shanghai Municipal Science and Technology Major Project (2018SHZDZX01), ZJ Lab, Shanghai Center for Brain Science and Brain-Inspired Technology, the young scientist project of MOE innovation platform, and the China Postdoctoral Science Foundation (2023M730712). Part of the experimental work was carried out in the Fudan Nanofabrication Laboratory.

Author contributions

Project and experiment design: E.S., L.T., J. Liu, Z.W., and L.Z. Device fabrication and characterization: Z.W., J. Liu, and E.S. Finite element simulations: J. Liu, Z.W., and P.L. *In vitro* and *in vivo* test: Z.W., J. Liu, Y. Shen, and Z.L. Biocompatibility evaluation: Y. Shao. Deep learning models: J. Liu and J. Liang. Guidance: E.S., B.H., M.W., Z.D., T.C., F.X., S.J., M.H., L.T., and Y.M. Writing draft: E.S., J. Liu, L. Z., Z.W., X.W., J. Liang, and L.T.

Competing interests
The authors declare no competing interests.

Additional information
Supplementary information The online version contains supplementary material available at https://doi.org/10.1038/s41528-025-00518-0.

Correspondence and requests for materials should be addressed to Lianjie Zhou, Ling Tao or Enming Song.

[1] Institute of Optoelectronics & College of Future Information Technology, College of Intelligent Robotics and Advanced Manufacturing, Shanghai Frontiers Science Research Base of Intelligent Optoelectronics and Perception, Fudan University, Shanghai, China. [2]State Key Laboratory of Integrated Chips and Systems, Fudan University, Shanghai, China. [3]International Institute for Intelligent Nanorobots and Nanosystems & State Key Laboratory of Surface Physics, College of Intelligent Robotics and Advanced Manufacturing, Fudan University, Shanghai, China. [4]Department of Nutrition and Food Hygiene, School of Public Health, Institute of Nutrition, Fudan University, Shanghai, China. [5]School of Biomedical Engineering, Shanghai Jiao Tong University, Shanghai, China. [6]Department of Ophthalmology, Tongji Hospital, School of Medicine, Tongji University, Shanghai, China. [7] State Key Laboratory of Materials for Integrated Circuits, Shanghai Institute of Microsystem and Information Technology, Chinese Academy of Sciences, Shanghai, China. [8] Institute of Mechanics and Computational Engineering, Department of Aeronautics and Astronautics, College of Intelligent Robotics and Advanced Manufacturing, State Key Laboratory of Coatings for Advanced Equipment, Fudan University, Shanghai, China. [9]State Key Laboratory of Medical Neurobiology and MOE Frontier Center for Brain Science, Institutes of Brain Science, Fudan University, Shanghai, China. [10]Department of Hand Surgery, National Clinical Research Center for Aging and Medicine, Huashan Hospital, Fudan University, Shanghai, China. [11]Department of Biomedical Engineering, College of Future Technology, Peking University, Beijing, China. [12]Zhejiang Key Laboratory of Extreme Environment Functional Materials, Yiwu Research Institute of Fudan University, Yiwu, Zhejiang, China. [13]Brain-Computer Interface Research, Fudan University, Shanghai, China. [14]These authors contributed equally: Junhan Liu, Zhongyuan Wu, Lianjie Zhou. ✉e-mail: ljzhou@fudan.edu.cn; ling_tao@fudan.edu.cn; sem@fudan.edu.cn